Available online at www.sciencedirect.com

ScienceDirect

Procedia CIRP 110 (2022) 36–40

www.elsevier.com/locate/procedia

V CIRP Conference on Biomanufacturing

Experimental And Numerical Investigation Of Large Strain Extrusion Machining Of AZ31 Magnesium Alloy For Biomedical Applications

M.R. Saffioti*[a], R. Bertolini[b], D. Umbrello[a], A. Ghiotti[b], S. Bruschi[b]

[a]*Department of Mechanical, Energy and Management Engineering, University of Calabria, 87036 Rende, CS, Italy*
[b]*Department of Industrial Engineering, University of Padova, Via Venezia 1, 35131, Padova, Italy*

* Corresponding author. Tel.: +39 0984 494637; fax: +39 0984 494637. *E-mail address:* mariarosaria.saffioti@unical.it

Abstract

Magnesium alloys represent promising bioresorbable orthopedic materials thanks to their biocompatibility, non-toxicity, and mechanical properties that are pretty close to the ones of the human bone. Nevertheless, the major drawback that impairs their widespread adoption in the biomedical field is represented by their unsatisfactory corrosion resistance once placed in the human body environment.
Several research studies have demonstrated that an effective method to control the degradation rate of magnesium alloys is represented by a proper conditioning of the surface characteristics of the alloy. With this in mind, the present work proves the feasibility of using Large-Strain Extrusion Machining (LSEM), namely a hybrid cutting–extrusion process, as a strategy to sensibly affect the surface features of the AZ31 magnesium alloy, and, as a consequence, its corrosion performances. The microstructure and micro-hardness close to the machined surface was investigated after LSEM. The experimental results were exploited to develop, calibrate and validate numerical simulations able to describe the microstructural and mechanical phenomena that occur under LSEM. The proposed approach shows that the simulation model can represent a useful tool to predict the magnesium alloy machining performances, thus reducing the need for numerous and time-consuming experimental tests to a great extent.

Keywords: AZ31 magnesium alloy; Biomaterials; Numerical simulation; Large strain extrusion machining.

1. Introduction

Magnesium alloys are recently in spotlight within the biomedical field because of the advantages they offer like biocompatibility and mechanical properties very similar to the ones of the human bones. Thanks to their biosafety within the human body along with their natural degradation rate in physiological environment, they can be used for manufacturing temporary orthopaedic and cardiovascular implants devices that does not require secondary removal surgery operations [1].

Nevertheless, the main limitation of the magnesium alloys is represented by the fact that their degradation inside the human body occurs faster than the one expected for the bone correct recovery, possibly leading to a premature failure of the biomedical device.

In this framework, recent research studies dealing with clinical applications of magnesium alloys have mainly concerned the development of strategies to reduce their corrosion degradation rate. Severe Plastic Deformation (SPD) processes have emerged as a potential way for manufacturing materials with Ultra Fined Grain (UFG) microstructure assuring enhanced mechanical and corrosion properties [2]. Among the available SPD processes, machining-based ones, like Large Strain Extrusion Machining (LSEM), are more and more attracting the researchers' attention because they are already foreseen in the process chain, without providing additional costs for manufacturing the product.

10.1016/j.procir.2022.06.009

LSEM refers to a simultaneous cutting and extrusion process, which converts the chip into a sheet with a desired and a priori controlled thickness [3]. In contrast to conventional machining, the extrudate thickness (*tc*) can be set smaller than the depth of cut (*t*), thus inducing large plastic strains and high hydrostatic pressure levels in the cutting zone. In a previous study of the Authors [4], LSEM was proved to be suitable to induce a significant deformation on the machined surface of an AZ31 magnesium alloy bar. As a matter of fact, an SPD layer, harder and more refined SPD compared to the annealed alloy, was found. These microstructural and mechanical alterations corresponded to an improvement of the corrosion resistance of the alloy, by shifting the related corrosion curves towards higher potentials and lower current densities. Besides to this, significant corrosion improvements were found also for the continuous chips that were obtained, as described in [5].

Considering the aforementioned positive, but preliminary, results, a further optimization of the process is needed. To this aim, an accurate numerical model of the LSEM process can greatly reduce costly and time-consuming machining trials and allows predicting the surface characteristics on the basis of the chosen cutting parameters.

Phenomenological material constitutive models, like the Johnson–Cook model, are the most used for describing the flow stress in Finite Element (FE) machining simulations, but, for a reliable description of the phenomena occurring during cutting and prediction of the surface integrity changes, they need to be integrated with additional models dealing with the workpiece microstructural evolution. In [6], a numerical model was built to predict the residual stresses variation after dry and cryogenic machining of the AZ31 magnesium alloy, showing that the model predictive capability was limited, being discrepancies among the experimental and numerically predicted values. A step forward was made in [7], in which a user subroutine was developed to predict the formation of affected layers induced by machining based on the dynamic recrystallization mechanism of the AZ31B alloy.

However, both the aforementioned studies neglect additional material-related phenomena, like twinning, which may drastically affect the surface condition in the case of magnesium alloys. In [8], a dislocation density-based constitutive model was developed to model the AZ31 microstructure evolution as well as the slip and twinning responses during a two-pass cryogenic machining operation. Results show that, compared to the experimental data, the numerical model was able to successfully capture the trend of the microhardness depth profile from the machined surface, the residual stress state and even the slip/twinning transition and resolved twinning lamellas.

Nevertheless, there is no publication on modeling surface changes during LSEM of magnesium alloys. In this context, a Johnson–Cook material constitutive law, considering both the microstructure and mechanical response, was developed and applied to the AZ31 alloy. The material model was implemented through a user subroutine using the DEFORM™ 2D FE software to predict the final distributions of various surface attributes after LSEM. The validity of the model was then witnessed on the basis of grain size and microhardness measurements gained from experimental LSEM trials.

2. LSEM experiments

Fig. 1 shows a scheme of the LSEM process. The LSEM setup is composed by a cutting tool and a constraint placed above it, which represents the peculiarity of the operation with respect to conventional orthogonal cutting. In this way, a combined machining-extrusion process takes place and the chip thickness is reduced from *t* to t_c. On this basis, the chip compression ratio (λ) is calculated as $\lambda = t/t_c$.

In LSEM, the shear deformation (γ) is highly localized and imposed in a narrow zone idealized as a shear plane and calculated by Eq. (1):

$$\gamma = \frac{\lambda}{cos\alpha} + \frac{1}{\lambda * cos\alpha} - 2 * tan\alpha \qquad (1)$$

where α stands for the tool rake angle.
According to Eq. (1), various strain can be imposed by varying α and λ.

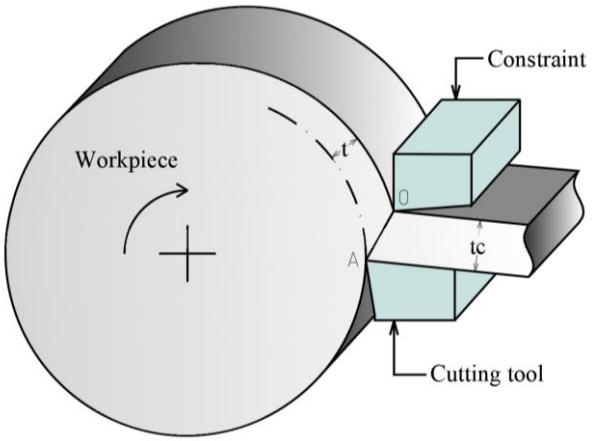

Figure 1. Scheme of the LSEM process.

The material under investigation is the AZ31 magnesium alloy supplied in form of a bar of 60 mm of diameter. The material is characterized by an equiaxed microstructure with an average grain size of 15 μm (Fig. 2).

The LSEM experiments were performed on AZ31 5-mm thick discs using an orthogonal cutting setup on a Mori Seiki NL 1500™ CNC lathe. More details of the experimental cutting procedure can be found in [4]. The adopted cutting insert was a commercial uncoated semi-finishing insert VBMW160404H13A characterized by $\alpha = 0°$. The other LSEM conditions were the following: t= 0.3 mm, λ= 1.1 and V= 120 m/min. It is worth noting that, the presence of the constraint above the tool prevents any temperature recording through a thermo-camera. Thus, the temperature resulting from the simulation was not comparable due to the absence of experimental measurements.

After LSEM, metallographic investigations were carried out on samples extracted from both the chips and the LSEM bar in correspondence of its surface. All these samples were firstly cold mounted, polished and finally etched by immersing them in acid picric solution for 2 min to reveal the microstructural features that were captured using optical microscopy.

The Leitz™ Durimet microhardness tester was used to measure the Vickers microhardness with a load of 98 mN for 30 s following the ASTM E92-17 standard. Three values were recorded for each measurement and then the average calculated. Indentations were taken every 20 μm from the machined surface till a depth of 420 μm in the case of machined bar and across the section of the LSEM chip.

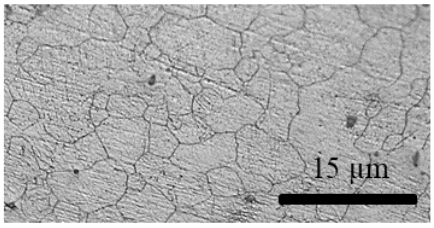

Fig. 2. AZ31 microstructure in the as-delivered condition.

3. Numerical modelling

The numerical procedure developed in this work employs a FE based thermo-mechanical model formulation of the LSEM process. A 2D plane-strain simulation was carried out using SFTC DEFORM 2D™ where the material constitutive models reported in the following were implemented in FORTRAN™ and ran as user subroutine. In the following the main characteristics of the LSEM numerical model are described.

- The Johnson-Cook equation (Eq. 2 in Fig. 3) is exploited as material constitutive law. The model provides the equivalent stress σ at varying deformation rate $\dot{\varepsilon}$ and temperature T. More details about this model can be found in [7]. Along with the Johnson-Cook model, the Hall-Petch equation (Eq. 3 in Fig. 3) is introduced to consider the effect of the strain hardening, ascribable to the grain size variation during the process, to the yield strength A. Table 1 reports the values of the material constants of the above reported models on the basis of the available literature data [4, 8, 9].
- The semi-empiric approach proposed in [10] is used to model the dynamic recrystallization phenomenon (from Eq. 4 to Eq. 9 in Fig. 3). The mechanical and thermal contributions are taken into account through the Zener-Hollomon parameter Z (Eq. 4 in Fig. 3). When a critical value of deformation ε_{cr} is achieved (Eq. 7 in Fig. 3), the dynamic recrystallization of the material takes place and the amount of dynamically recrystallized grains X_{DRX} is calculated (Eq. 6 in Fig. 3) on the basis of the equivalent strain for 50% recrystallized fraction $\varepsilon_{0.5}$ (Eq. 8 in Fig. 3). The average grain size D is calculated as a weighted average among the initial grain size D_0 and the recrystallized grain size D_{DRX} (Eq. 5 and Eq. 9 in Fig. 3, respectively).
- A mathematical model for dislocations motion (from Eq. 10 to Eq.13 in Fig. 3) is implemented to estimate the density of dislocations on the basis of the process temperature T, initial dislocation density ρ_0 and deformation rate $\dot{\varepsilon}$. Table 2 reports the values of the material constants for grain size and dislocation density evolutions on the basis of the available literature data [4, 8, 9].
- The hardness of the machined bar and chips (Eq. 15 in Fig. 3) is then calculated as the sum of different contributions, namely the material initial hardness HV_0, the Hall-Petch hardness ΔHV_{HP} and the Taylor hardness ΔHV_{dis}. ΔHV_{HP} accounts for the grain boundary role in hindering dislocation motion whereas ΔHV_{dis} accounts for the dislocation density variation during the process. To apply the model, the shear modulus changes as a function of temperature were incorporated from the data provided in [11].
- The workpiece was modelled as an elastoplastic body and meshed with 20000 elements. DEFORM™ 2D meshing method allows defining a finer mesh at the workpiece-tool interface, which 6 μm in this case. The cutting tool was modelled as a rigid body and meshed with 5000 elements while the rigid constraint was meshed with 1000 elements.
- The temperatures of the workpiece, cutting tool and constraint were set equal to the environment temperature, namely 20°C. The heat exchange with the environment was kept fixed using a global heat transfer coefficient equal to 10^5 kW/(m^{2}K). The tool-workpiece friction coefficient as well as the constraint-workpiece one were set equal to 0.7 according to [12].

MATERIAL CONSTITUTIVE MODEL

Johnson-Cook Flow Stress

$$\sigma = [(A + B(\varepsilon^n)]\left[1 + C * ln\left(\frac{\dot{\varepsilon}}{\dot{\varepsilon}_0}\right)\right]\left[1 - \left(\frac{T - T_0}{T_m - T_0}\right)^m\right] \quad (2)$$

Hall-Petch Strengthening

$$A = A_0 + \frac{K_{HP}}{\sqrt{D}} \quad (3)$$

Grain size evolution

$$Z = \dot{\varepsilon} * e^{\frac{Q}{RT}} \quad (4)$$

$$D = D_{DRX} * X_{DRX} + D_0(1 - X_{DRX}) \quad (5)$$

$$X_{DRX} = 1 - e^{-0.704*(\frac{\varepsilon - \varepsilon_{cr}}{\varepsilon_{0.5}})^{2.144}} \quad (6)$$

$$\varepsilon_{cr} = 0.0152 * {D_0}^{0.1965} * Z^{0.0453} \quad (7)$$

$$\varepsilon_{0.5} = 0.0706 * \dot{\varepsilon}^{0.0483} * {D_0}^{0.399} * e^{\frac{275.17}{T}} \quad (8)$$

$$D_{DRX} = 4073.4 * Z^{-0.198} \quad (9)$$

Dislocation density evolution

$$\frac{\partial \rho}{\partial \varepsilon} = U - \Omega\rho \quad (10)$$

$$\rho_i = \rho_{i0} * e^{-\Omega*\varepsilon} + \frac{U}{\Omega}(1 - e^{-\Omega*\varepsilon}) \quad (11)$$

$$U = 10 * 10^{13} * \dot{\varepsilon}^{0.17} * e^{0.17\frac{134000}{RT}} \quad (12)$$

$$\Omega = 17.7 * \dot{\varepsilon}^{-0.17} * e^{-0.17\frac{134000}{RT}} \quad (13)$$

Output

$$\sigma = \left[A_0 + \frac{K_{HP}}{\sqrt{D}} + B(\varepsilon^n)\right]\left[1 + C * ln\left(\frac{\dot{\varepsilon}}{\dot{\varepsilon}_0}\right)\right]\left[1 - \left(\frac{T - T_0}{T_m - T_0}\right)^m\right] \quad (14)$$

$$\Delta HV_{tot} = HV_0 + \Delta HV_{HP} + \Delta HV_{dis} = HV_0 + C(\frac{K_{HP}}{\sqrt{D}} + \alpha G(T) b\sqrt{\rho_i}) \quad (15)$$

Fig. 3. Constitutive laws implemented in the LSEM numerical model.

Table 1. Material constants of the Johnson-Cook and Hall-Petch equations (Eq. 2 and Eq. 3).

Parameter description	Symbol	Value
Hardening coefficient	B (MPa)	321.3
Hardening factor	n	0.13
Strain rate sensitivity coefficient	C	0.016
Plastic deformation reference	ε_0	1
Room temperature	T_0(°C)	20
Melting temperature	T_m (°C)	650
Softening coefficient	(m)	1.829
Yield stress	A_0 (MPa)	125
Hall-Petch constant	K_{HP}	$2.10E^{+02}$

Table 2. Material constants of the grain size and dislocation density evolution equations (from Eq. 4 to Eq. 15).

Parameter description	Symbol	Value
Gas constant	R ($J*K^{-1}*mol^{-1}$)	8.31
Activation energy	Q (kJ/mol)	178831
Initial grain size	D_0 (µm)	15
Initial dislocation density	ρ_0 (m^{-2})	$1E^{14}$
Recovery function	Ω	$2.92E^{-4}$
Burger's vector	b (m)	$3.21E^{-10}$

The overall details concerning the setting of the simulation and the assignment of the mesh, boundary conditions, velocity, temperature and contact area are visible in Fig. 4.

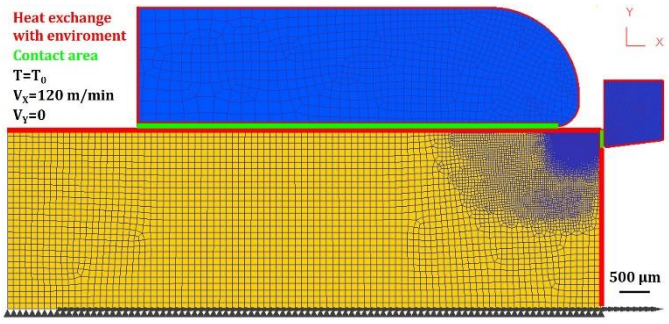

Fig. 4. Mesh and boundary conditions for the LSEM numerical model.

4. Results

Fig. 5 (a) and (b) show the long continuous chip (called herein strip) obtained after the LSEM process and the cross-section microstructure in correspondence of its center, respectively. The LSEM process leads to the formation of defects-free strips thanks to the superimposition of elevated pressure and temperature in the deformation zone, guaranteed by the presence of the constraint. The strip is characterized by a homogeneous and equiaxed microstructure, emblematic of the dynamic recrystallization that occurred at the shear plane AO (see Fig. 1).

Fig. 6 shows the comparison between the measured and predicted microstructural characteristics, namely grain size and micro-hardness measured along the strip section. It can be seen that the predicted values of grain size and micro-hardness fit correctly the experimental data, being the differences equal to -5% and 14%, respectively.

Indeed, the Fig. 7 shows that hardness is the highest in the correspondence of the surface and gradually decreases moving away from it, recovering the bulk value at a certain distance below the surface. The comparison between the experimental and numerically predicted microhardness of the LSEM bar is shown in Fig. 8. The hardness prediction from the numerical model shows a remarkable agreement with the experimental results up to a distance of 40 µm from the surface, showing a difference of solely 6% on average. On the contrary, an underestimation of 16% on average is registered in the zone ranging from 60 µm to 320 µm below the machined surface.

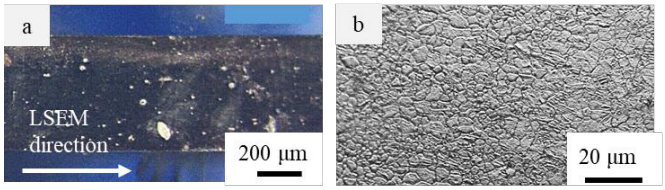

Figure 5. Morphology (a) and cross-section microstructure (b) of the continuous chips obtained during the LSEM process.

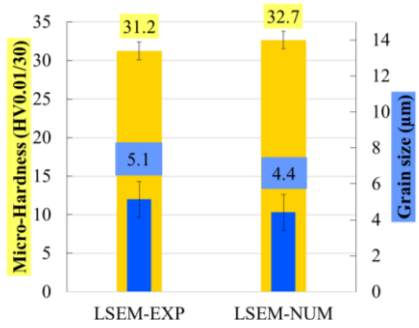

Fig. 6. Comparison between experimental (EXP) and numerically predicted (NUM) microhardness and grain size of the LSEM strip.

Finally, Fig. 7 (a) shows the workpiece subsurface deformation after LSEM. In general, an SPD layer composed of grains characterized by a high density of deformation twins and sub-grains, underlying the machined surface, is readily visible.

The SPD layer thickness (*d*) was equal to t= 32.6 ± 2.1 µm. To such microstructure alteration corresponds an alteration of micro-hardness values, as numerically predicted in Fig. 7 (b).

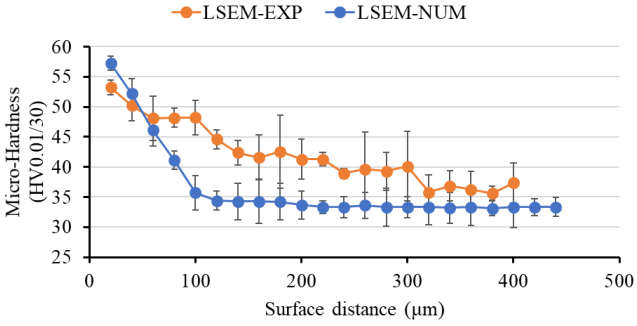

Fig. 7. Comparison between experimental (EXP) and numerically predicted (NUM) microhardness of the LSEM bar.

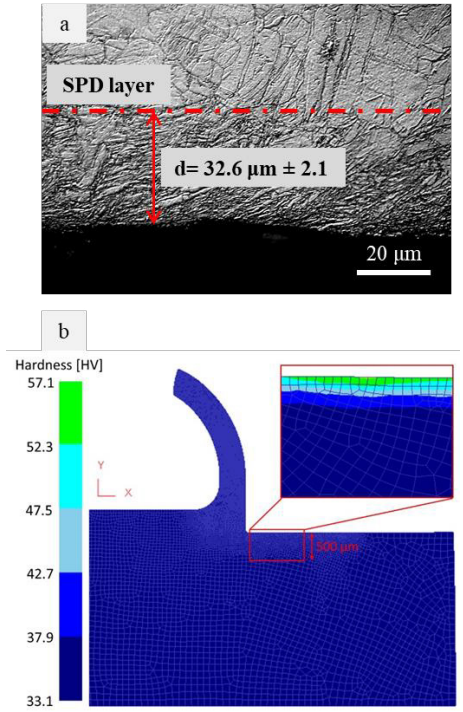

Fig. 8. Microstructure (a) and numerically predicted microhardness (b) in the bar subsurface after LSEM.

5. Conclusions

This paper has presented a FE model of the Large-Strain Extrusion Machining (LSEM) process carried out on AZ31 magnesium alloy bars.

The Johnson-Cook constitutive law combined with physically-based models was employed to describe the material flow stress and the microstructural phenomena occurring during the process. The numerical model was calibrated on the basis of literature data and validated by comparing the numerical outcomes with the ones from LSEM trials. In particular, the grain size and micro-hardness of the LSEM strips as well as the micro-hardness below the surface of the LSEM bar were compared, showing a good fitting.

Future works will be dedicated to the numerical optimization of the LSEM process parameters to obtain the most suitable conditions that can favor a corrosion resistance improvement of the machined part.

Acknowledgements

This research was supported by Ministry of Education, University and Research - MIUR within the PRIN 2017 project “Surface functionalization to improve triBo-corrosIOn performaNces of metal Implants through advanCed machining operations - BIONIC” (Project code: 201742RB8R).

References

[1] Nan L, Zheng Y. Novel magnesium alloys developed for biomedical application: a review. J Mater Sci Technol 2013; 29.6: 489-502.
[2] Kasaeian-Naeini M, Sedighi M, Hashemi R. Severe plastic deformation (SPD) of biodegradable magnesium alloys and composites: A review of developments and prospects. J Magnesium Alloys 2021; article in press.
[3] Efe M, Moscoso W, Trumble KP, Compton WD, Chandrasekar S. Mechanics of large strain extrusion machining and application to deformation processing of magnesium alloys. Acta Mater 2012;60(5): 2031-42.
[4] Bertolini R, Bruschi S, Ghiotti A. Large strain extrusion machining under cryogenic cooling to enhance corrosion resistance of magnesium alloys for biomedical applications. Procedia Manuf, 2018;26:217-27.
[5] Bertolini R, Bruschi S, Ghiotti A, Pezzato L, Dabalà M. Large strain extrusion machining of magnesium alloys for biomedical applications. Procedia Cirp 2018;71:105-10.
[6] Outeiro JC, Rossi F, Fromentin G, Poulachon G, Germain G, Batista AC. Process mechanics and surface integrity induced by dry and cryogenic machining of AZ31B-O magnesium alloy. Procedia Cirp 2013;8:487-92.
[7] Pu Z, Umbrello D, Dillon Jr OW, Lu T, Puleo DA, Jawahir IS. Finite element modeling of microstructural changes in dry and cryogenic machining of AZ31B magnesium alloy. J Manuf Process 2014; 16(2): 335-343.
[8] Shen N, Ding H, Pu Z, Jawahir IS, Jia T. Enhanced surface integrity from cryogenic machining of AZ31B Mg alloy: a physics-based analysis with microstructure prediction. J Manuf Sci Eng 2017;139(6).
[9] Lee S, Ham HJ, Kwon SY, Kim SW, Suh CM. Thermal conductivity of magnesium alloys in the temperature range from -125 C to 400 C, Int J Thermophys 2014; 34/12:2343–2350.
[10] Qin YJ, Pan QL, He YB, Li WB, Liu XY, et al. Modeling of flow stress for magnesium alloy during hot deformation, Mater Sci Eng 2010; 527/10–11:2790–2797.
[11] Huang K, Logé RE. A review of dynamic recrystallization phenomena in metallic materials, Materials and Design 2016; 111:548–574.
[12] Filice L, Micari F, Rizzuti S, Umbrello D. A critical analysis on the friction modelling in orthogonal machining. Int J Mach Tool Manuf 2007;47(3–4): 709–14.